Performance Analysis of TiO$_2$-Modified Co/MgAl$_2$O$_4$ Catalyst for Dry Reforming of Methane in a Fixed Bed Reactor for Syngas (H$_2$, CO) Production

Arslan Mazhar [1], Asif Hussain Khoja [1,*], Abul Kalam Azad [2,*], Faisal Mushtaq [3], Salman Raza Naqvi [4], Sehar Shakir [5], Muhammad Hassan [5], Rabia Liaquat [5] and Mustafa Anwar [5]

[1] Fossil Fuels Laboratory, Department of Thermal Energy Engineering, U.S.-Pakistan Centre for Advanced Studies in Energy (USPCAS-E), National University of Sciences & Technology (NUST), Sector H-12, Islamabad 44000, Pakistan; arslanmazhar52@gmail.com

[2] School of Engineering and Technology, Central Queensland University, 120 Spencer Street, Melbourne, VIC 3000, Australia

[3] Department of Chemical Engineering, Faculty of Engineering & Architecture, Balochistan University of Information Technology, Engineering and Management Sciences, Airport Road, Baleli, Quetta 87300, Pakistan; faisalqta1977@gmail.com

[4] School of Chemical and Materials Engineering (SCME), National University of Sciences & Technology (NUST), Sector H-12, Islamabad 44000, Pakistan; salman.raza@scme.nust.edu.pk

[5] Department of Energy Systems Engineering, U.S.-Pakistan Centre for Advanced Studies in Energy (USPCAS-E), National University of Sciences & Technology (NUST), Sector H-12, Islamabad 44000, Pakistan; sehar@uspcase.nust.edu.pk (S.S.); hassan@uspcase.nust.edu.pk (M.H.); rabia@uspcase.nust.edu.pk (R.L.); mustafa@uspcase.nust.edu.pk (M.A.)

* Correspondence: asif@uspcase.nust.edu.pk (A.H.K.); a.k.azad@cqu.edu.au (A.K.A.)

Abstract: Co/TiO$_2$–MgAl$_2$O$_4$ was investigated in a fixed bed reactor for the dry reforming of methane (DRM) process. Co/TiO$_2$–MgAl$_2$O$_4$ was prepared by modified co-precipitation, followed by the hydrothermal method. The active metal Co was loaded via the wetness impregnation method. The prepared catalyst was characterized by XRD, SEM, TGA, and FTIR. The performance of Co/TiO$_2$–MgAl$_2$O$_4$ for the DRM process was investigated in a reactor with a temperature of 750 °C, a feed ratio (CO$_2$/CH$_4$) of 1, a catalyst loading of 0.5 g, and a feed flow rate of 20 mL min^{-1}. The effect of support interaction with metal and the composite were studied for catalytic activity, the composite showing significantly improved results. Moreover, among the tested Co loadings, 5 wt% Co over the TiO$_2$–MgAl$_2$O$_4$ composite shows the best catalytic performance. The 5%Co/TiO$_2$–MgAl$_2$O$_4$ improved the CH$_4$ and CO$_2$ conversion by up to 70% and 80%, respectively, while the selectivity of H$_2$ and CO improved to 43% and 46.5%, respectively. The achieved H$_2$/CO ratio of 0.9 was due to the excess amount of CO produced because of the higher conversion rate of CO$_2$ and the surface carbon reaction with oxygen species. Furthermore, in a time on stream (TOS) test, the catalyst exhibited 75 h of stability with significant catalytic activity. Catalyst potential lies in catalyst stability and performance results, thus encouraging the further investigation and use of the catalyst for the long-run DRM process.

Keywords: dry reforming of methane; TiO$_2$; MgAl$_2$O$_4$; syngas; hydrothermal process

1. Introduction

The rising concerns over greenhouse gas (GHG) emissions on global warming and climate change has motivated many industrial production facilities to reconsider plans on how to effectively control and recycle GHGs to produce synthetic fuels [1,2]. Synthesis gas (mainly made of H$_2$ and CO) is a vital fuel gas mixture currently being employed as an alternative to petroleum-based fuels. Syngas is considered the primary feedstock in the production of some important liquid fuels, such as ammonia and methanol, and it can also

be used as an intermediate resource to produce H_2, synthetic petroleum, and hydrocarbon products [3–5].

Syngas can be produced from various routes and techniques. The catalytic reforming technologies for syngas production, such as the steam reforming of methane (SRM) [6], partial oxidation of methane (POM) [5], and dry reforming of methane (DRM) [7,8], have gained much importance in recent years [9,10]. The DRM has been shown to be a promising technique that employs two major GHGs (CH_4 and CO_2) as feedstock to produce syngas [11,12]. The H_2/CO syngas ratio produced above unity as a result of the DRM reaction is favourable for the synthesis of value-added chemicals and long-chain hydrocarbons for Fischer–Tropsch (FT) synthesis [13]. The DRM converts stable molecules of CO_2 and CH_4 via catalytic pathways into syngas when mixed in-unit proportion (Equation (1)).

$$CH_4 + CO_2 \rightarrow 2\,CO + 2\,H_2 \; \Delta H^{\circ}_{25°C} = 247 \text{ kJ mol}^{-1} \; (\text{ DRM }) \tag{1}$$
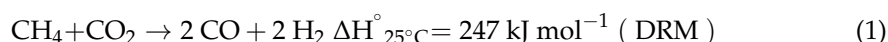
The DRM has some notable disadvantages, as it promotes reverse water-gas shift reaction (RWGS) and carbon formation via methane decomposition [14,15]. RWGS mainly occurs when the H_2 to CO ratio becomes less than unity. The carbon formation is expressed by the famous Boudouard reaction, which can result in the deactivation of catalysts [16,17] Equations (2) and (3).

$$CH_4 \rightarrow C + H_2 \; \Delta H^{\circ}_{25°C} = 75 \text{ kJ mol}^{-1} \; (\text{Methane cracking}) \tag{2}$$

$$2\,CO \rightarrow C + CO_2 \; \Delta H^{\circ}_{25°C} = -172 \text{ kJ mol}^{-1} \; (\text{Boudouard reaction}) \tag{3}$$
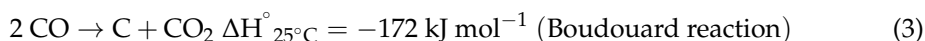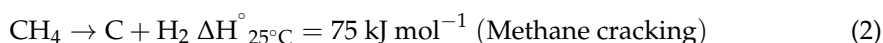
It is understood that carbon formation has adverse effects on the reaction mechanism and results in carbon deposition, thus leading to the deactivation of catalysts that affect the reaction lifetime and altering the H_2/CO ratio [18,19]. To have a better understanding of coke formation, understanding the thermodynamics of the DRM is important for commercial DRM process implementation. Thus, the development of a catalyst with a high catalytic performance and resistance to coking is an important objective [20]. In this regard, catalyst performance depends on active metal and support properties, their interaction, and their catalytic behaviour.

In the catalytic DRM, noble metals like rhodium (Rh), palladium (Pd), and ruthenium (Ru) are recognised as stable catalysts that can inhibit carbon formation but are commercially unviable [21–23]. Nickel (Ni) is the most widely used commercially active metal due to its availability and good catalytic activity. The carbon deposition rate and sintering of the Ni catalyst still need to be addressed in the DRM [24–26]. Cobalt (Co) exhibits a better stability to carbon deposition, but its performance in the DRM must be improved [27–30]. For instance, El et al. [31] investigated the effects of confinement on the catalytic performance of two silica supports (SiO_2 and SBA-15) on Co loading. The results indicated that Co/SBA-15 showed stability against the sintering of mesopores during the DRM and that the addition of rhodium to Co/SBA-15 led to increased stability and activity with less carbon coking.

The effect of the support on the catalyst depends on the nature of the support, which can play an essential role in the activity and stability of the catalyst [32]. $MgAl_2O_4$ is an excellent support material with a high sintering resistance, good hydrothermal stability, and excellent mechanical strength [3,14,33]. During the DRM, CO_2 dissociation and adsorption proceed at a faster rate with the use of basic support, and, in this regard, $MgAl_2O_4$ can be used as a support material due to its basic nature and high surface area [34–36]. DRMs done using different Ni loadings on nanocrystalline $MgAl_2O_4$ (with its high surface area) have shown high catalytic activity and stability, with an increase in carbon deposition following the increase in Ni loading [14,37].

Bi-support catalysts can be very effective in improving mechanical properties and catalytic performance. For example, TiO_2 provided some favourable properties for the DRM [38]. The strong metal–support interaction between the TiO_2 support and metal exhibited a high resistance towards coke deposition while increasing catalyst activity and

stability. The activity and stability of TiO_2 can be improved using a structured TiO_2-based catalyst [38,39]. In catalysis, a higher catalytic activity has been observed with the use of metal supported on TiO_2 nanowires. The use of a low-temperature SRM using Ni/TiO_2 as a catalyst revealed that stronger metal–support interactions assisted low-temperature methane activation while Ni species aided in hydrogen production via WGSR. It was reported that Ni/TiO_2 showed an enhanced coking resistance [40]. Though TiO_2 nanowires have been investigated for other photocatalytic and fuel cell applications, their effect on the DRM with a combination of the Co transition metal and added bi-support has yet to be investigated [41]. The combination of TiO_2 and $MgAl_2O_4$ as co-supports and Co as an active metal could enhance the CH_4 and CO_2 activation, resist carbon formation, and aid stability.

In this study, the catalytic performance of a TiO_2 nanowire-modified $Co/MgAl_2O_4$ catalyst was investigated for the DRM in a fixed bed reactor. Co/TiO_2–$MgAl_2O_4$ was synthesised by the co-precipitation process, the hydrothermal method, and the wetness impregnation method. The catalyst was characterised using various techniques such as XRD, SEM, EDS, TGA, and FTIR. The catalyst was tested for the DRM activity and the effect of metal loading, and stability tests were conducted for longer times on stream (TOS). Furthermore, the spent catalyst was characterised by XRD, SEM-EDS, and TGA to analyse the carbon formation during the TOS and to present a possible reaction mechanism.

2. Materials and Methods

2.1. Synthesis of $MgAl_2O_4$ and TiO_2 Nanoparticles

To prepare the $MgAl_2O_4$ spinel, a modified co-precipitation method followed by the hydrothermal process was used, as shown in Figure 1a. A stoichiometric amount of Mg $(NO_3)_2 \cdot 6H_2O$ (99.99%, Sigma Aldrich) and Al $(NO_3)_3 \cdot 9H_2O$ (98%, Honeywell Fluka) was added in deionised water and set to mild stirring conditions until a homogeneous solution formed. An ammonia solution (32%) was used as a precipitating agent, which was added dropwise into the solution with continuous stirring to maintain a pH of at 10.5 because higher PH would have resulted in a lower crystallite size and a higher specific surface area [42]. The stirring and heating continued until the stabilisation of the pH at 10.5 and the appearance of a milky white solution. The solution was then transferred to a hydrothermal autoclave maintained at 160 °C for 24 h and left to cool at room temperature overnight. The precipitates were separated using a centrifuge and washed with warm DI water and absolute ethanol until the pH of the solution reached 7.0 [14]. The slurry was dried at 110 °C overnight. The prepared sample was a ground and calcined in a furnace maintained at 800 °C for 5 h in static air. The collected sample was ground until fine $MgAl_2O_4$ particles were formed.

In the typical synthesis of TiO_2 nanowires (NWs), 0.70 g of titanium (IV) oxide (99%, Sigma-Aldrich) nano-powder were added in 70 mL of a 10 M solution of NaOH and continuously stirred until the formation of a homogeneous solution. The solution was then shifted to a hydrothermal autoclave, heated to 160 °C for 5 h, and allowed to cool at room temperature. The solution was centrifuged to collect the white precipitates, and then it was washed with a 0.1 M HCl solution and warm deionised water several times to bring the pH to 7.0 [43]. The sample was oven-dried at 110 °C, followed by calcination at 500 °C to obtain a fine white powder.

2.2. Preparation of Co/TiO_2–$MgAl_2O_4$ Nanocomposite

A schematic representation of Co/TiO_2–$MgAl_2O_4$ nanocomposite preparation is shown in Figure 1a. For the preparation of the Co/TiO_2–$MgAl_2O_4$ nanocomposite, the wetness impregnation method was used with the addition of $Co(NO_3)_2 \cdot 6H_2O$ (98%, Merck) on $MgAl_2O_4$ and TiO_2 NW supports. In catalyst preparation, 1.0 g of $MgAl_2O_4$ and 0.1 g of TiO_2 NWs were dispersed in a 0.1 M $Co(NO_3)_2 \cdot 6H_2O$ solution and allowed to stir for 5 h at 110 °C. The resulting slurry was oven-dried at 110 °C overnight and calcined at 750 °C for

5 h. The prepared sample was named 5%Co/TiO$_2$–MgAl$_2$O$_4$. Similarly, composite samples of 2.5 and 7.5% Co loading were prepared.
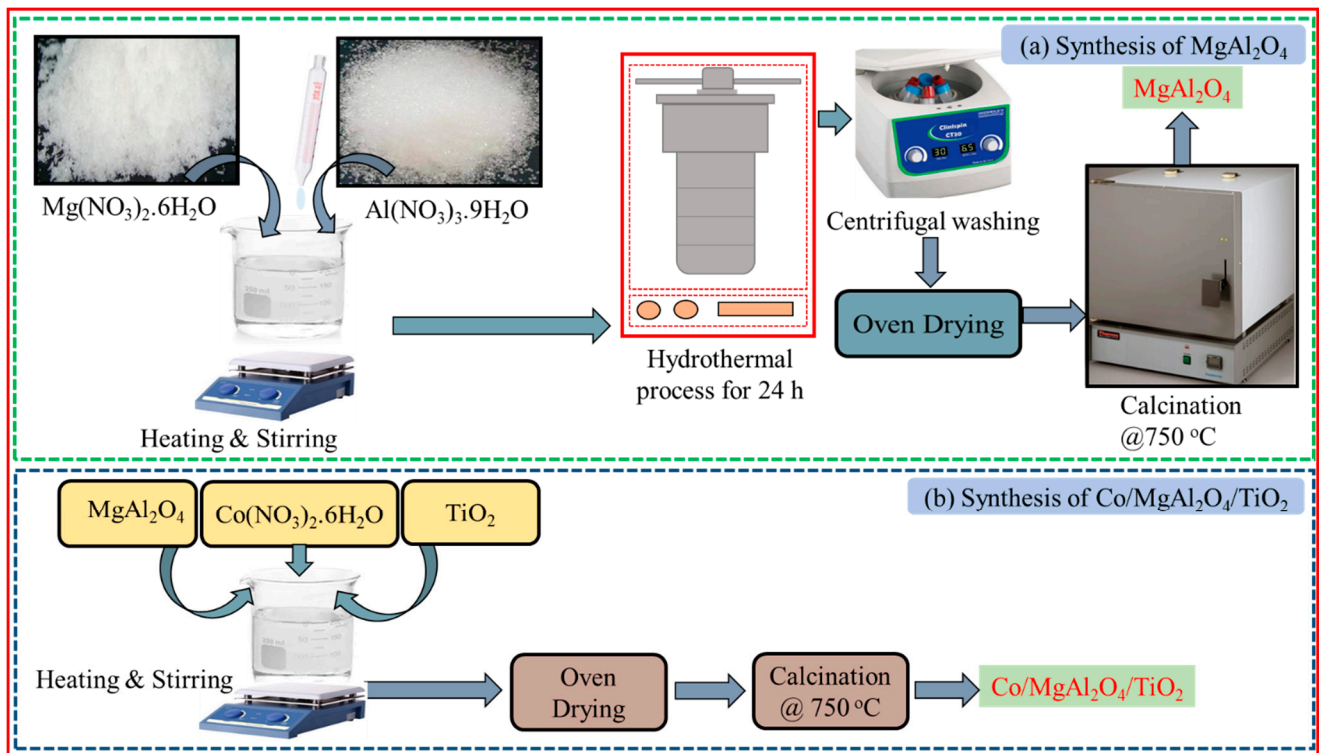

Figure 1. Schematic representation of catalyst preparation (**a**) synthesis of MgAl2O4 (**b**) synthesis of Co/TiO$_2$-MgAl$_2$O$_4$

2.3. Materials Characterisation

The crystalline structure and phase transition of the prepared catalysts were analysed by the X-ray diffraction method. The identification of the peaks of the calcined and ground samples was carried out via a Bruker D8 advanced X-ray diffractometer with an irradiation wavelength of 1.5418 Å at 40 kV and 40 mA operating conditions. XRD patterns were obtained using diffraction angles over the range of 5–90° with a step size of 0.05°. The Scherrer equation was used to estimate the average crystallite size [44].

The surface morphology of the prepared fresh samples and the spent samples were examined by SEM. To obtain the micro-level images of the samples, a JSM-6490A JEOL SEM (Japan) was used. The resolution of the microscope was set to 3 nm, and it was operated at 30 kV. EDX was used to analyse the elemental composition of catalyst.

TGA was performed using a TGA 5500 from TA Instruments (USA) to observe the thermal stability of the fresh catalyst and the amount of carbon deposited on spent samples by maintaining a nitrogen flow of 25 mL min^{-1} and a heating rate of 10 °C min^{-1} to a maximum temperature at 900 °C. The weight of the sample used for the analysis was 10 mg. The percentage of weight loss was observed at different temperatures based on the reactive carbon.

FTIR was used to identify the functional groups in the sample and the interactions between them. The FTIR analysis was carried out on a Cary 630 FTIR (Agilent Technologies, USA), with the wavenumber ranging from 4000 to 650 cm^{-1}.

2.4. Experimental Setup

The experimental setup scheme for the DRM is illustrated in Figure 2. The fixed bed reactor of PARR (Model # LSP-2.38-0-32-1C-2335EEE, Moline USA) was used for the DRM process. The reactor consisted of a 2.5 ft SS-316 material tube with a $\frac{1}{2}$ inch diameter. Th tube openings were fixed with SS RED union at both ends and connected to a gas mixer.

The supply of the feed gas was controlled with digital MF4600 series mass flow controllers. The reactor temperature was controlled by the 4871 Series Process Controllers. The K-type thermocouple was used to control the temperature of the catalyst bed. The catalyst was sandwiched in between the glass wool and kept in the centre of the reactor using suitable support. Before each experiment, 60 mL min^{-1} of N_2 were introduced to purge the reactor system, and 20 mL min^{-1} of H_2 in the presence of 60 mL min^{-1} of N_2 gas were used to reduce the catalyst at 750 °C for 1 h by activating the active sites due to the requirement of higher conversions and longer stability runs for the DRM. During experimental runs, the mass flow rates of the feed gas CH_4 (99.99%) and CO_2 (99.99%) were controlled at 10 mL min^{-1} each and then introduced into the reactor that was set at 750 °C and 0.5 g of catalyst loading. The reaction products were allowed to pass through the condenser before gas analysis. The gases were analysed with a gas chromatograph (GC 2010 plus Shimadzu) equipped with a thermal conductivity detector (TCD) [45]. The temperature of the GC column was set at 200 °C, while the peak retention time was set for 10 min.
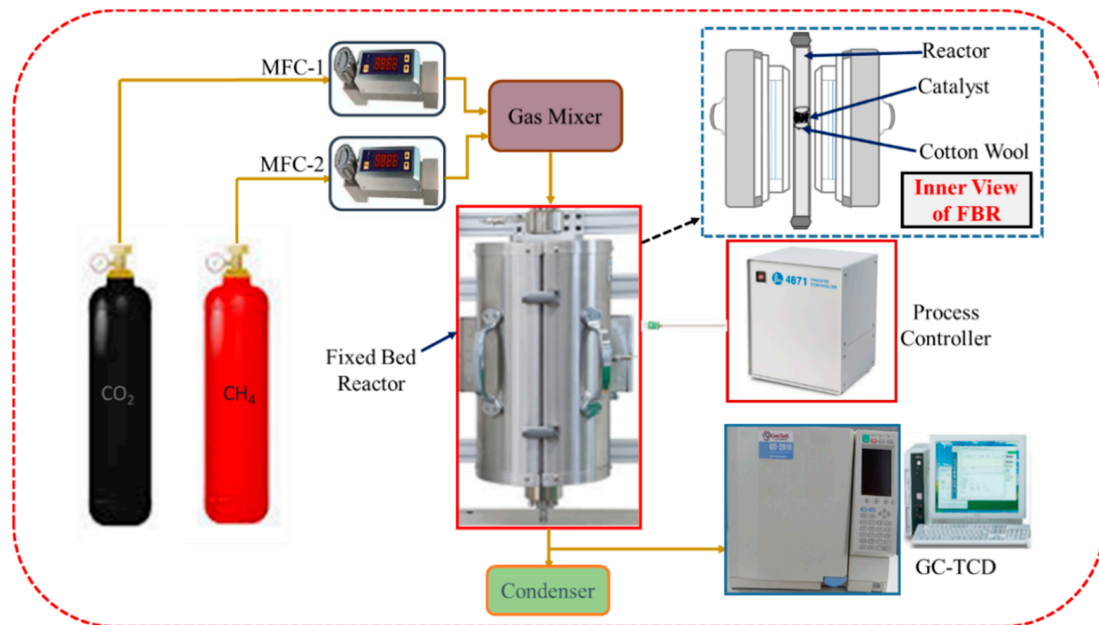

Figure 2. Schematic representation of the DRM experimental setup.

2.5. Catalytic Activity Calculations

Catalytic activity tests were conducted to analyse the performance and stability of the DRM catalyst in the fixed bed reactor. The DRM activity test included reactant conversion, selectivity, and yield, as presented in Equations (4)–(10). The term 'n' represents the number of moles in the following equations.

$$CH_4 \text{conversion} \left(X_{CH_4} \right)\% = \left[\frac{(nCH_4)_{\text{converted}}}{(nCH_4)_{\text{feed}}} \times 100 \right] \tag{4}$$

$$CO_2 \text{conversion} \left(X_{CO_2} \right)\% = \left[\frac{(nCO_2)_{\text{converted}}}{(nCO_2)_{\text{feed}}} \times 100 \right] \tag{5}$$

$$H_2 \text{selectivity} \left(S_{H_2} \right)\% = \left[\frac{(nH_2)_{\text{produced}}}{(2 \times nCH_4)_{\text{converted}}} \times 100 \right] \tag{6}$$

$$CO \text{selectivity} \left(S_{CO} \right)\% = \left[\frac{(nCO)_{\text{produced}}}{(nCH_4 + nCO_2)_{\text{converted}}} \times 100 \right] \tag{7}$$

$$H_2 \text{yield} \left(Y_{H_2} \right)\% = \left[\frac{(nH_2)_{produced}}{2 \times (nCH_4)_{feed}} \times 100 \right] \tag{8}$$

$$CO \text{yield} (Y_{CO})\% = \left[\frac{(nCO)_{produced}}{(nCH_4 + nCO_2)_{feed}} \times 100 \right] \tag{9}$$

$$H_2/CO \text{ ratio} = \left[\frac{(nH_2)_{produced}}{(nCO)_{produced}} \right] \tag{10}$$

3. Results and Discussion

3.1. Characterization of Catalyst

The XRD of the prepared samples is shown in Figure 3. $MgAl_2O_4$ (PDF:21-1152) showed diffraction peaks centred at $2\theta = 31.27°$, $36.85°$, 44.8, and $65.2°$ corresponding to different planes with intensified characteristic peaks at $36.85°$ (hkl;311) with a d-spacing of 0.243 nm and at $65.2°$ (hkl; 440) with a d-spacing of 0.14 nm, thus indicating the presence of a spinel phase of $MgAl_2O_4$ [46,47]. A rutile phase with a tetragonal symmetry was detected for TiO_2 (PDF:21-1276) diffraction peaks, with the major phase (211) observed at $54.32°$ and a d-spacing of 0.16 nm [48]. Upon adding cobalt with $MgAl_2O_4$, some peaks observed in $MgAl_2O_4$ XRD went missing due to the merging of peaks with the neighbour peaks. Similarly, cubic phase $CoAl_2O_4$ (PDF:44-0160) showed a major peak at $36.7°$ (hkl; 311) with a d-spacing 0.244 nm and a space group of 227:Fd3m, while the other peaks observed at $31.74°$ and $44.63°$ with the corresponding planes of (220) and (400), respectively [49]. Diffraction peaks were observed at $31.2°$ and $36.8°$ with planes (220) and (311), respectively, with a space group of 227:Fd3m of the cubic phase, thus indicating the presence of Co_3O_4 (PDF:43-1003) [50]. $CoTiO_3$ (PDF:15-0866), with a hexagonal phase with a major peak observed at $32.8°$ (hkl; 104) and a d-spacing of 0.27 nm, showed the space group of R-3(148) [51].
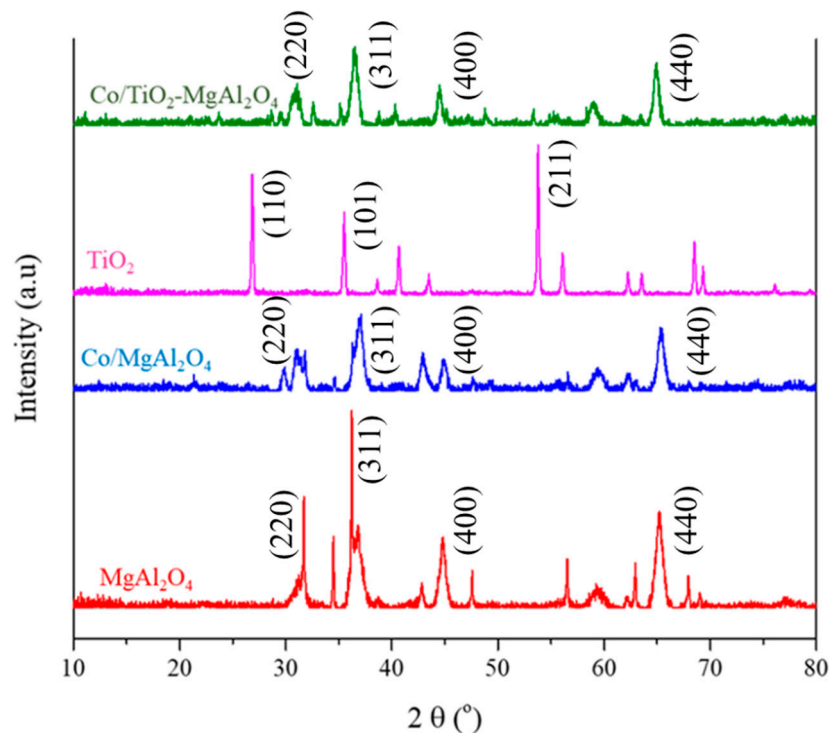
Figure 3. XRD analysis of prepared $MgAl_2O_4$, $Co/MgAl_2O_4$, TiO_2, and $Co/TiO_2-MgAl_2O_4$ samples.

An SEM micrograph of $MgAl_2O_4$ particles is shown in Figure 4a,b, which indicates the formation of porous-structure, block-shaped crystallites depicting the sintering of

particles because of the higher temperature calcination. Figure 4c,d demonstrates the formation of mixed, very fine TiO_2 particles and TiO_2 nanowires due to the hydrothermal method [52]. Figure 4e,f indicates the modification of $MgAl_2O_4$ particles, while Co and TiO_2 dispersed over the surface and extended to the pores, ultimately showing a mixed composite structure. The EDXs for $MgAl_2O_4$, TiO_2, and $Co/TiO_2–MgAl_2O_4$ are presented in Figure 5a–c. The possible compounds are present in the spectrum, and the extra peaks are associated with carbon tape and gold, that were added during coating before the EDX analysis. The Co loading was confirmed by EDX, as it was presented in the composite.
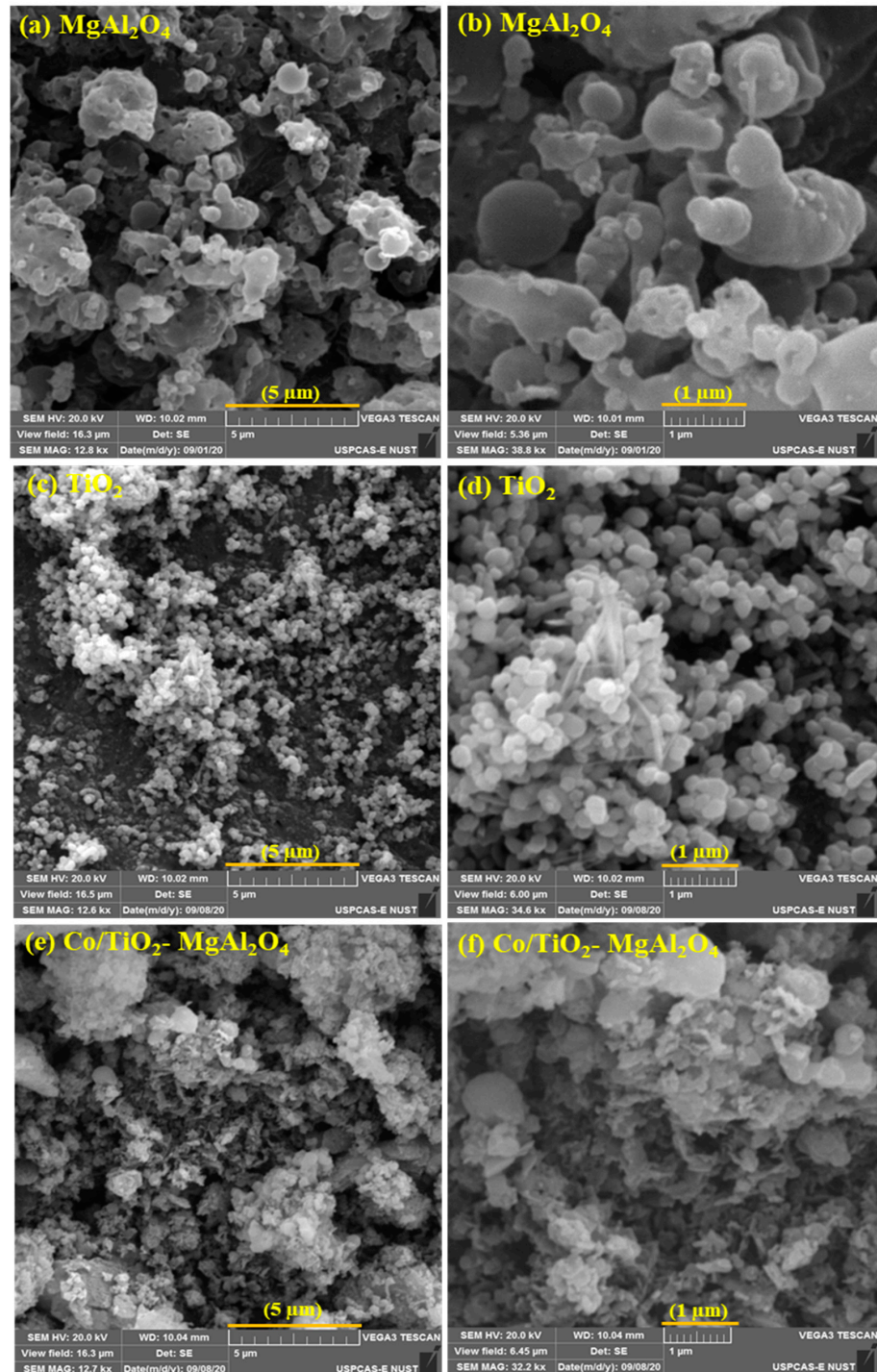

Figure 4. SEM images of prepared fresh samples: (**a**,**b**) 5 and 1 µm of $MgAl_2O_4$, (**c**,**d**) 5 and 1 µm of TiO_2, and (**e**,**f**) 5.0 and 1.0 µm of $Co/TiO_2–MgAl_2O_4$.
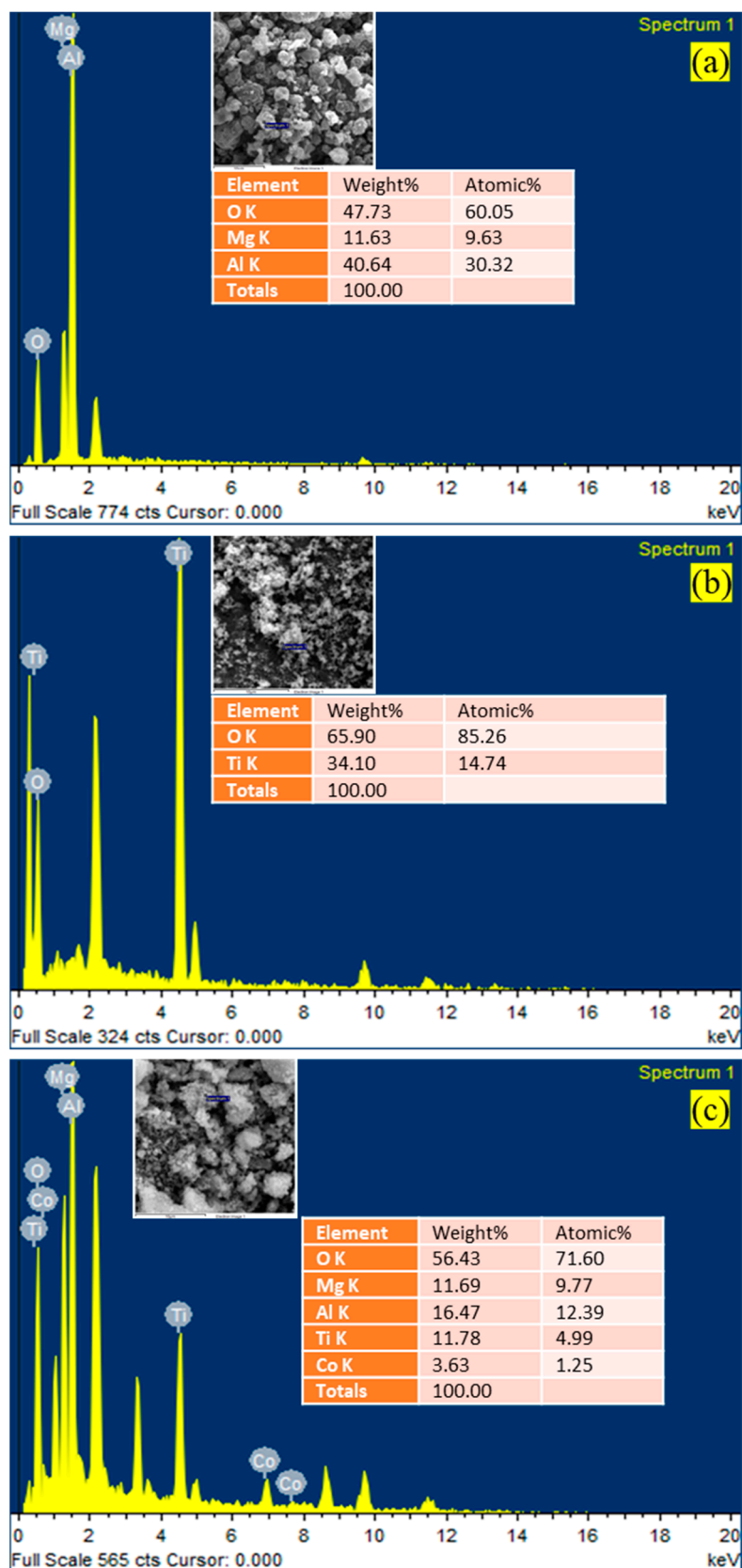
Figure 5. EDS analysis of fresh samples: (**a**) $MgAl_2O_4$, (**b**) TiO_2, and (**c**) 10 Co/TiO_2–$MgAl_2O_4$.

Figure 6 shows the thermal stability of the prepared samples. A total of 5% weight loss was observed in the $MgAl_2O_4$ sample TGA analysis, as shown in Figure 6a. A weight

loss of 3.5% was observed up to 250 °C because the material was subjected to the removal of the adsorbed moisture and the combustion of nitrates that went unreacted during the reaction, while the rest of the weight loss was due to the dihydroxylation of the mixed oxide to oxides [14]. Furthermore, the TGA analysis of the TiO_2 sample showed a minimal weight loss of up to 2%, thus exhibiting the stability of the sample, and the weight loss was due to adsorbed moisture removal and the decomposition of organic compounds (as presented in Figure 6b), while the slight weight gain after 600 °C was attributed to the rearrangement of the particles after impurity removal and reaction completion. The TGA of the fresh Co/TiO_2–$MgAl_2O_4$ nanocomposite showed a gradual weight loss up to 5% with the increase in temperature, most of which was rooted in moisture removal, while the sudden weight loss at a high temperature was due to the decomposition of bonds and the formation of the intermediate complexes of a composite, as presented in Figure 6c [14].
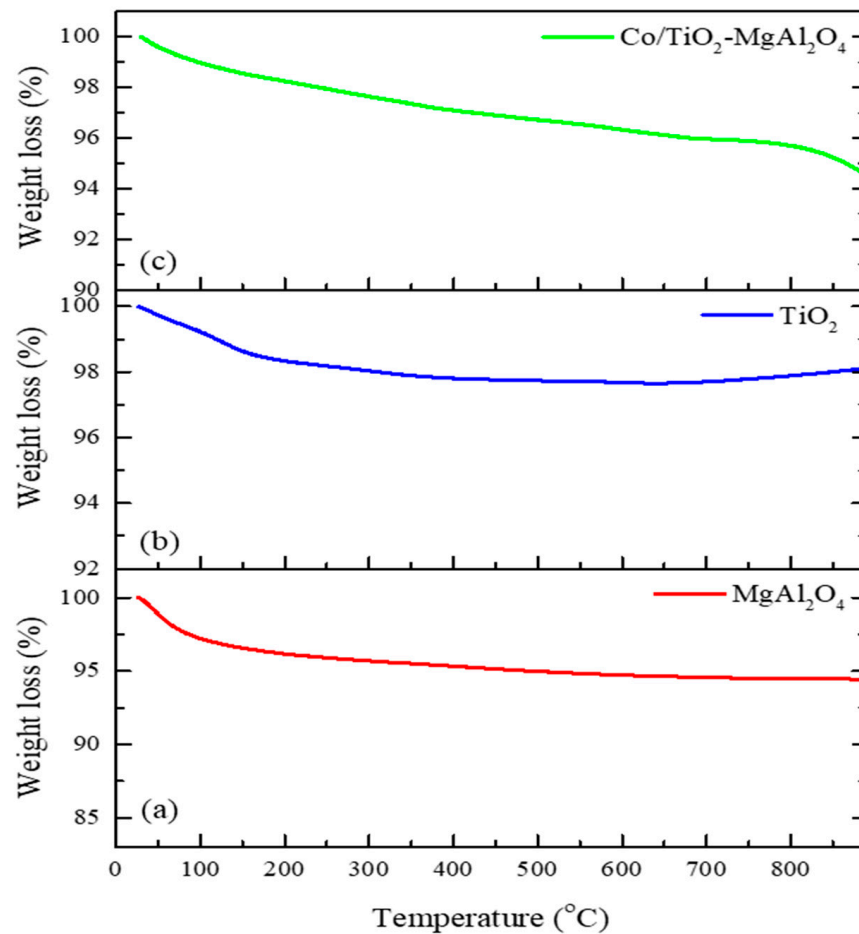

Figure 6. TGA analysis of prepared fresh samples: (**a**) $MgAl_2O_4$, (**b**) TiO_2, and (**c**) Co/TiO_2–$MgAl_2O_4$.

The FTIR analysis of the prepared fresh samples is shown in Figure 7. The IR spectrum of calcined $MgAl_2O_4$ observed at 912 cm^{-1}, which corresponded to the stretching vibration of Mg–O–Al falling into inorganic bands and Al–O bonds, was indicative of the crystal $MgAl_2O_4$ spinel [53–55]. With Co/TiO_2–$MgAl_2O_4$, two peaks identified at 900 cm^{-1} corresponded to the vibration of Mg–O–Al, where the peak identified at 744 cm^{-1} corresponded to O–Ti–O bond stretching vibrations depicting an anatase morphology [56,57] because the band range of 500–800 cm^{-1} followed the anatase crystal vibration modes [58]. The presence of a small peak around 850 cm^{-1} corresponded to O–Co–O, which indicated the formation of Co_3O_4 [59]. In the IR spectrum of TiO_2, the small peak was slightly shifted below 700 cm^{-1}, which could have been related to the stretching vibration of Ti–O bonding.
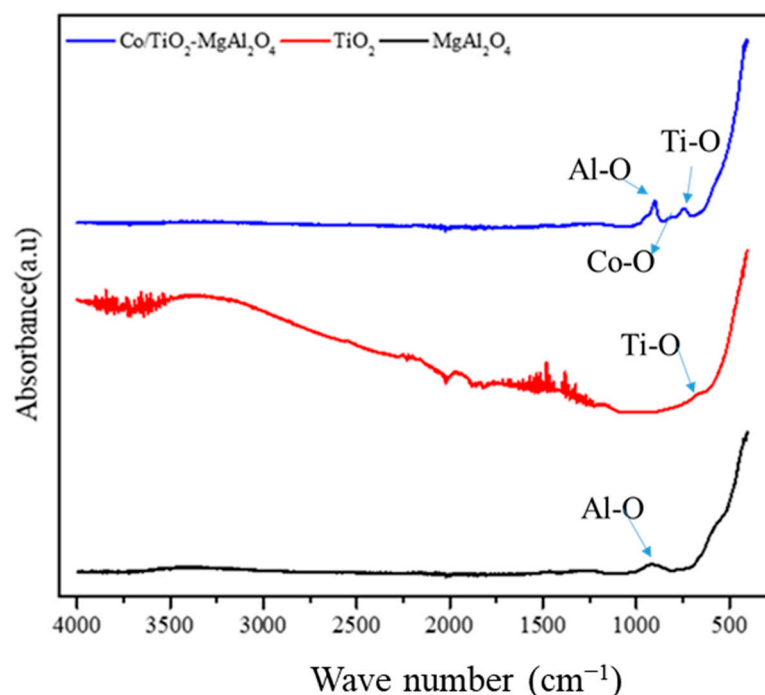
Figure 7. FTIR analysis of the prepared fresh samples.

3.2. Dry Reforming of Methane (DRM)

The prepared fresh catalyst samples were loaded into a fixed bed reactor to conduct activity and stability tests during the DRM process. The feed gas ratio was set to 1, with a flow rate of 20 mL min^{-1}, and it was fed to reactor maintained at 750 °C with a catalyst loading of 0.5 g.

3.2.1. Catalyst Activity Test

DRM activity test results for the $MgAl_2O_4$ and composites with different Co loading are shown in Figure 8a–c. For $MgAl_2O_4$, the conversions of CH_4 and CO_2 were recorded at 61% and 68.5%, respectively. The selectivities of H_2 and CO were observed at 17.5% and 26.5%, respectively, whereas the yields of H_2 and CO were calculated at 11% and 17%, respectively. The CH_4 conversion was observed to be less than the CO_2 conversion, while the higher CO_2 conversion could be attributed to the basic nature of the support that caused the activation of CO_2 [60]. For the Co/TiO_2–$MgAl_2O_4$, the increase in the conversion of CH_4 and CO_2 with Co loading could be associated with Co loading that showed a good interaction that formed $CoTiO_3$ and $CoAl_2O_4$ with supports, as depicted by the XRD analysis. The higher activity results were due to the higher amount of reduced surface Co sites with increases in cobalt loading [61]. The higher activity results coming with increases in Co loading corresponded with the reduction of Co_3O_4 at lower temperatures, and XRD analysis confirmed the presence of Co_3O_4 species. The conversions of CH_4 and CO_2 were recorded at 68% and 73%, respectively for the composite of 2.5% depicted in Figure 8a. In contrast, 5% of Co loading resulted in conversions of 73% and 78% for CH_4 and CO_2, respectively, while 7.5% of Co loading resulted in 76% and 83% yields of CH_4 and CO_2, respectively. A similar trend of increase was shown for H_2 and CO selectivity at 2.5–7.5% of Co loading. The highest H_2 and CO selectivities recorded for 7.5% of Co loading were 43% and 46.5%, respectively, as presented in Figure 8b. The yields of H_2 and CO remained 18% and 22%, respectively, for 2.5% of Co loading, and they were highest at 33% and 37%, respectively, for the 7.5% Co-loaded composite, as demonstrated in Figure 8b.
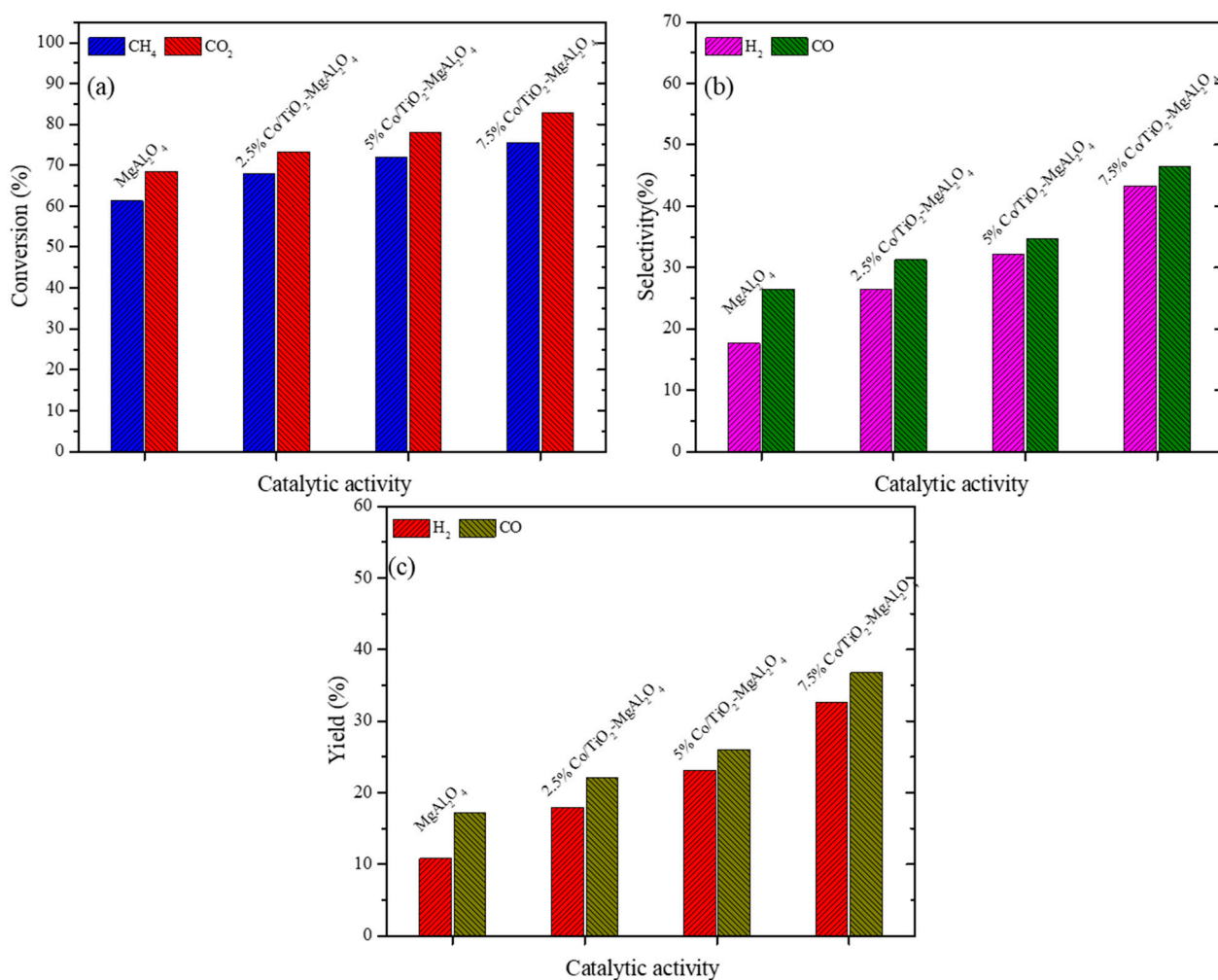
Figure 8. Co-loading effect over $TiO_2/MgAl_2O_4$: (**a**) conversion (X_{CH4} and X_{CO2}), (**b**) selectivity (S_{H2} and S_{CO}), and (**c**) yield (Y_{H2} and Y_{CO}). Catalyst loading = 0.5 g; reaction temperature = 750 °C; feed ratio (CO_2/CH_4) = 1; feed flow rate = 20 mL min^{-1}.

For the low Co-loaded composite, relatively lower conversions of CH_4 and CO_2 were observed, primarily due to the presence of $CoAl_2O_4$ species, as observed in the XRD analysis, and these were reducible at higher temperatures. However, higher Co-loaded composites had comparatively more easily reducible species, thus resulting in higher activity [62]. Though the higher Co loading adhered with the issue of carbon deposition because the larger amount of available carbon species led to deactivation, in this case, the highest conversions of the 7.5% Co-loaded composite was because of the balance provided by the higher CO_2 conversion that provided more oxygen species to the excess carbon formed by the CH_4 decomposition [27]. The higher conversion rates of CO_2 to CO and oxygen species due to fast reactions resulted in the reaction of the available oxygen species and the high amount of carbon produced with the CH_4 decomposition for the highly loaded Co. The result was more CO produced in comparison to H_2, as shown by the produced syngas ratio. The 7.5% Co-loaded composite, however, showed a gradual decrease in activity when tested for more extended-run stability tests. However, possible issues connected with high Co-loaded composites include the formation of cobalt clusters that affect support surface properties, and unfavourable gas adsorption conditions with the long-term stability analysis of the 7.5% Co-loaded composite led to the deactivation of the catalyst and, consequently, a lower catalytic activity with time [63]. Thus, considering the better activity and stability results, further tests for conversion, selectivity, yield, and a syngas ratio of over 75 h longer-run stability tests were only conducted for the 5% Co-loaded composite.

To better understand the role of the supports and active metal, as well as their effects on a fully developed catalyst, different catalysts like $MgAl_2O_4$, TiO_2, $Co/MgAl_2O_4$, Co/TiO_2, and Co/TiO_2–$MgAl_2O_4$ were tested for 5 h TOS for CH_4 and CO_2 conversions, as shown in Figure 9a,b, respectively. Additionally, the H_2 and CO selectivity and the H_2 and CO yield for the prepared catalysts are presented in Figure 10a,b and Figure 11a,b, respectively. The results indicated that TiO_2 resulted in the lowest CH_4 and CO_2 conversion, and the lowest selectivity and yield of H_2 and CO compared to other catalysts because TiO_2, in its pure form in the absence of metal, does not have a significant effect on conversion at higher temperatures but provides good metal–support interactions, as indicated by the formation of a $CoTiO_3$ intermediate while loading the Co and the provision of good stability [64]. For $MgAl_2O_4$ support, CH_4 conversion averaged 61%, while CO_2 conversion averaged approximately 70% over-range during the 5 h TOS, which indicated that inherent basic nature of the $MgAl_2O_4$ spinel provided good support and the combined use of Mg and Al could achieve good thermal stability [65]. The basic support aided the dissociation of CO_2 [66]. The results indicated that the use of an $MgAl_2O_4$ support could provide decent catalytic results. The lower conversion, selectivity, and yield corresponding to Co/TiO_2 were due to the metallic Co oxidation because the oxidation species (CO_2) caused catalyst deactivation [67,68]. $Co/MgAl_2O_4$ showed intermediate conversions of CH_4 and CO_2, with average values of 65% and 72%, respectively, which could mainly be associated with the formation of $CoAl_2O_4$, as discussed in the XRD analysis of $Co/MgAl_2O_4$, and was the reason for the inhibition of carbon deposition [69]. The 5% Co/TiO_2–$MgAl_2O_4$ composite showed the maximum conversions of CH_4 and CO_2, along with maximum H_2 and CO selectivity and yield. It is associated to good metal–support interactions that contributed to activity and provided good stability [39]. Due to its basic nature, the presence of the $MgAl_2O_4$ support in the composite resulted in CO_2 adsorption and dissociation that produced CO, while the cobalt in the composite aided CH_4 activation to produce more H_2 and surface carbon. The TiO_2 support played role in the reaction of $CoTiO_3$ species with surface carbon to avoid coke deposition.

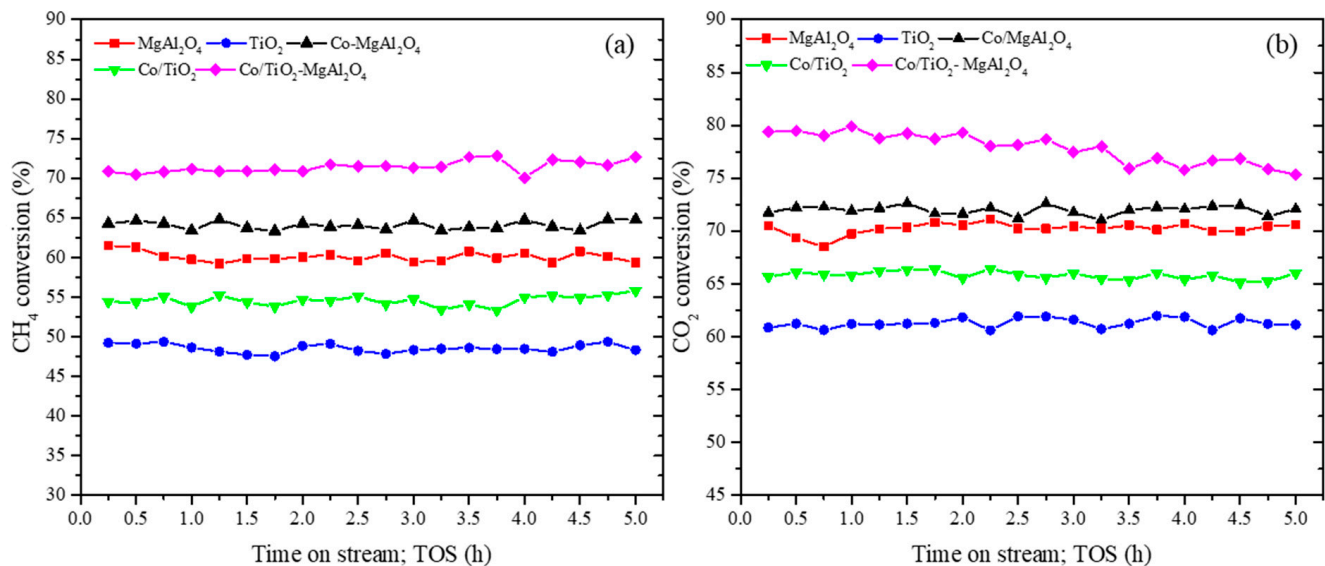**Figure 9.** Effect of time on stream: (**a**) CH_4 conversion and (**b**) CO_2 conversion over different prepared fresh samples. Catalyst loading = 0.5 g; reaction temperature = 750 °C; feed ratio (CO_2/CH_4) = 1; feed flow rate = 20 mL min^{-1}.
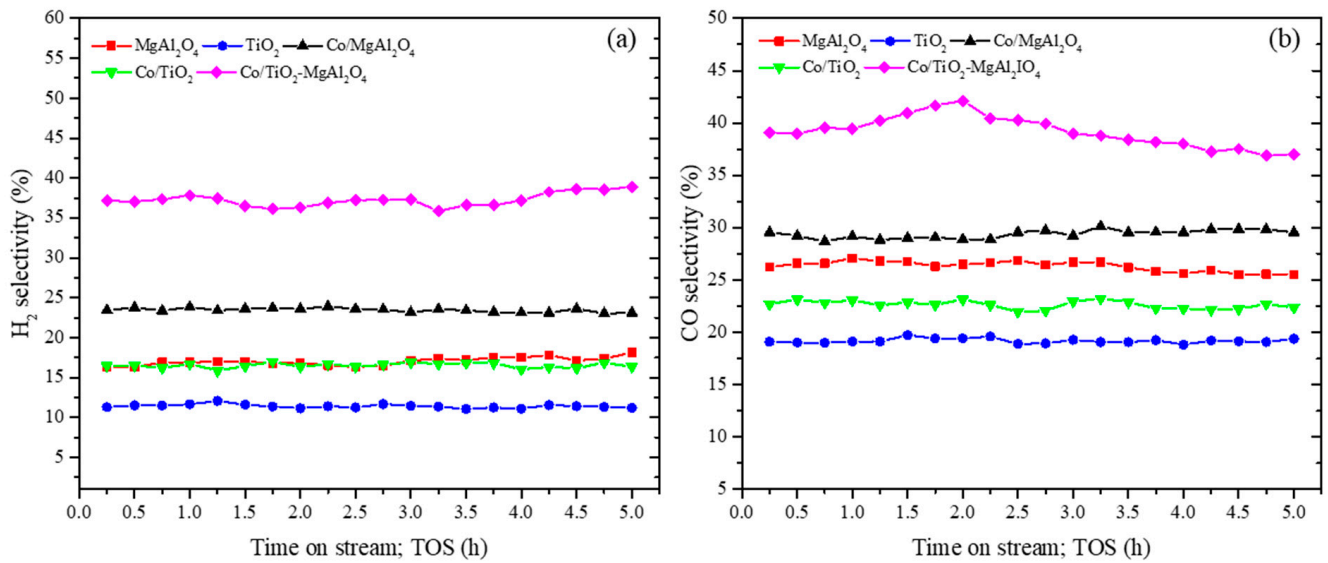
Figure 10. Effect of time on stream: (**a**) H_2 selectivity (S_{H2}) and (**b**) CO selectivity (S_{CO}) over different prepared fresh samples. Catalyst loading = 0.g; reaction temperature = 750 °C; feed ratio (CO_2/CH_4) = 1; feed flow rate = 20 mL min^{-1}.

Figure 11. Effect of time on stream: (**a**) H_2 yield (Y_{H2}) and (**b**) CO yield (Y_{CO}) over different prepared fresh samples. Catalyst loading = 0.5 g; reaction temperature = 750 °C; feed ratio (CO_2/CH_4) = 1; feed flow rate = 20 mL min^{-1}.
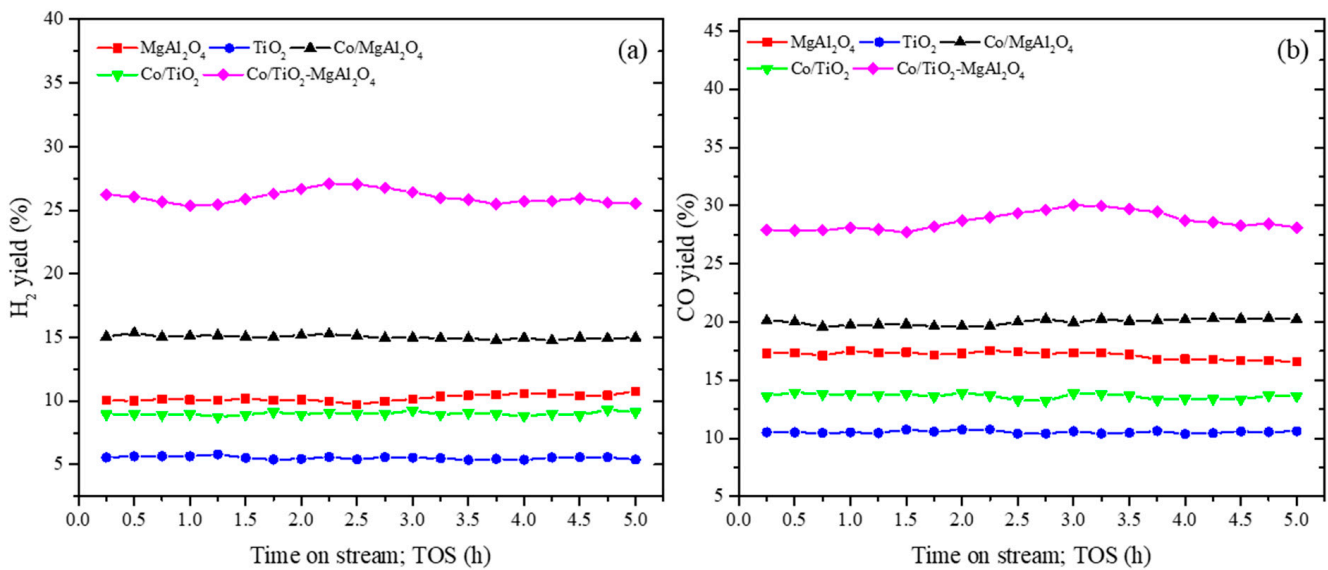
3.2.2. Stability Analysis of Composite

The 5%Co/TiO$_2$–MgAl$_2$O$_4$ was tested for stability analysis over the reaction time of 75 h under the same test conditions. Figure 12a demonstrates that the stability test showed a gradual increase in CO_2 and CH_4 conversion. The gradual rise was possibly due to the activation of some deposited carbon species. The selectivity of H_2 and CO, as presented in Figure 12b, showed the same trend with a gradual rise and then stabilisation for the next phase. The stability in activity was noticed for 75 h on TOS.
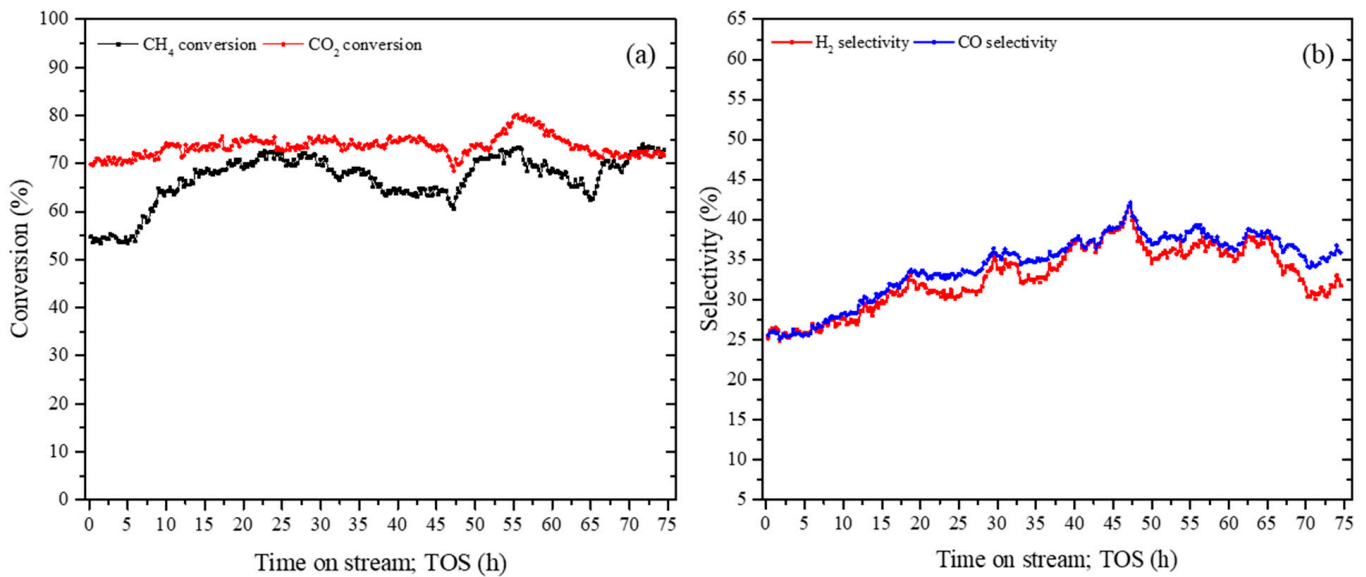
Figure 12. Time on stream vs. (**a**) conversion (X_{CH4} and X_{CO2}) and (**b**) selectivity (S_{H2} and S_{CO}) over 5% $Co/TiO_2–MgAl_2O_4$. Catalyst loading = 0.5 g; reaction temperature = 750 °C; feed ratio (CO_2/CH_4) = 1; feed flow rate = 20 mL min^{-1}.

The yield of H_2 and CO, as presented in Figure 13, showed similar trends to that of selectivity for the 75 h TOS. The H_2/CO ratio (Figure 13) value below unity and close to 0.9 was estimated for the 75 h TOS stability test. The H_2/CO ratio below unity showed a lower amount of carbon formation and good stability, as a relatively greater amount of CO was produced. The reasons for greater CO production were the faster reaction of carbon with CO_2 than CH_4 dissociation and the reaction of intermediate $CoTiO_3$ with carbon. Additionally, the possible reaction of H_2O produced due to the RWGS reaction (though was not physically observed) with C produced more H_2 and CO [70].
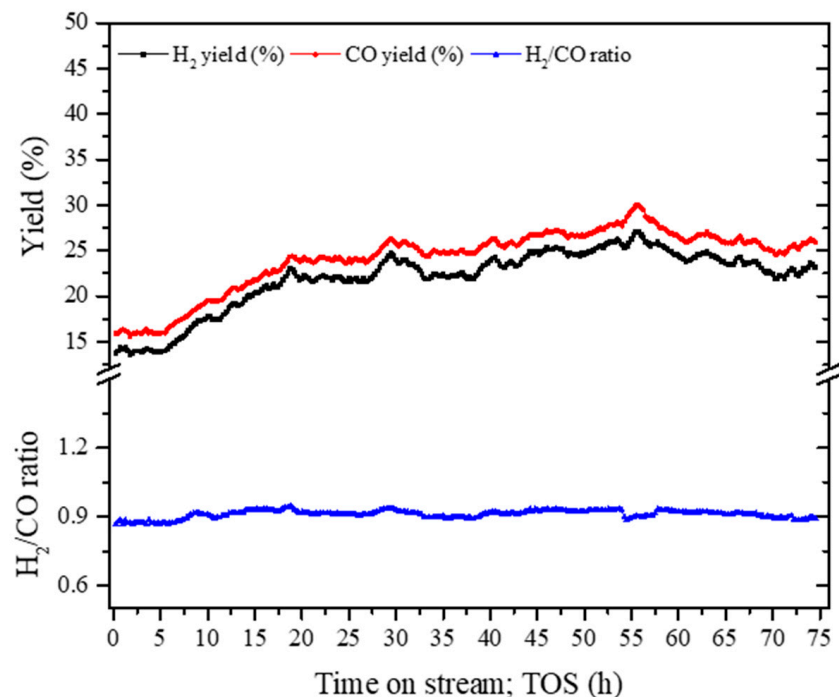

Figure 13. Time on stream vs. yield (Y_{H2} and Y_{CO}) and H_2/CO ratio over 5% $Co/TiO_2–MgAl_2O_4$. Catalyst loading = 0.5 g; reaction temperature = 750 °C; feed ratio (CO_2/CH_4) = 1; feed flow rate = 20 mL min^{-1}.

3.3. Characterisation of Spent Catalyst

The spent catalyst collected after 75 h of TOS was further analysed and characterised by XRD, TGA, SEM, and EDX. The results are shown in Figures 14 and 15 to investigate the carbon formation over the catalyst. Figure 14a shows that the XRD pattern of the spent catalyst confirmed the presence of the same crystalline phases as those observed in the fresh composite sample, having the same peaks of the $MgAl_2O_4$ spinel (PDF#21-1152) with a main peak at 36.85° (hkl; 311). TiO_2 (PDF#21-1276) was also observed as the same rutile phase with tetragonal geometry, and its main peak was slightly shifted at 51.8° (hkl; 211). A slight shift in the main peak of $CoAl_2O_4$ (PDF#44-0160) was observed at 36.0° (hkl; 311), while Co_3O_4 (PDF#43-1003) was identified in the fresh sample with peaks at 31.2° (hkl; 220) and 36.8° (hkl; 311). $CoTiO_3$ (PDF#15-0866) indicated a peak at 32.8° (hkl; 104), as observed in the fresh sample. The graphite carbon (PDF#41-1487) with a hexagonal geometry confirmed the peak at 26.3° (hkl; 002) with a d-spacing of 0.337 nm [71]. The TGA profile of the spent catalyst, as shown in Figure 14b, was analysed over three different temperature regions. Column I showed a total 4–5% weight loss up to 300 °C, which could be attributed to the moisture removal and other volatile species [72], where a significant weight loss of almost 14% was observed in column II in a temperature range of 300–500 °C due to the presence of reactive carbon species such as α-C and β-C [73]. Similarly, column III showed a 2–3% weight loss above 500 °C, which could be ascribed to a lower amount of filamentous carbon (γ-C) formation [3].
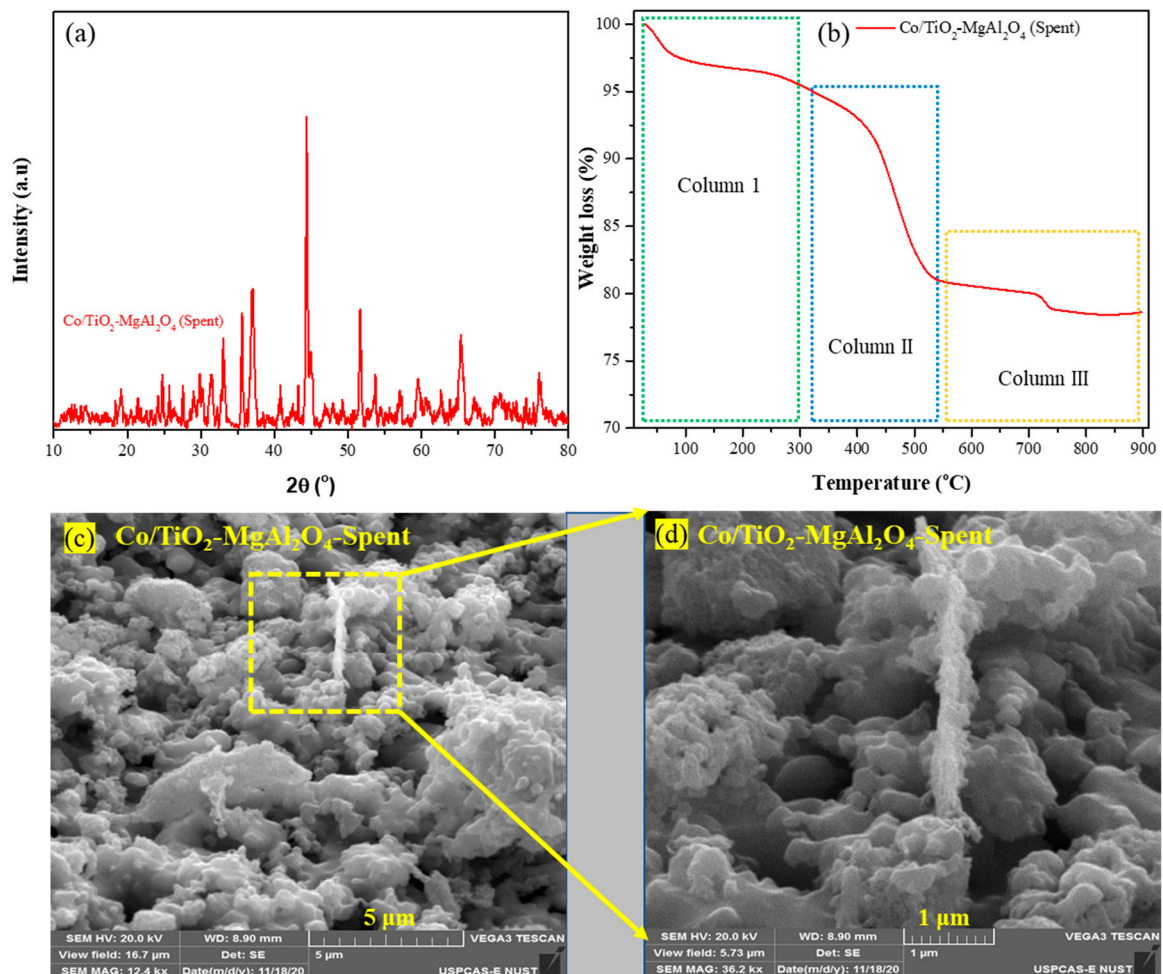

Figure 14. Spent catalyst characterization: (**a**) XRD micrograph, (**b**) TGA analysis, and (**c**,**d**) SEM analysis at 5 and 1 μm, respectively.
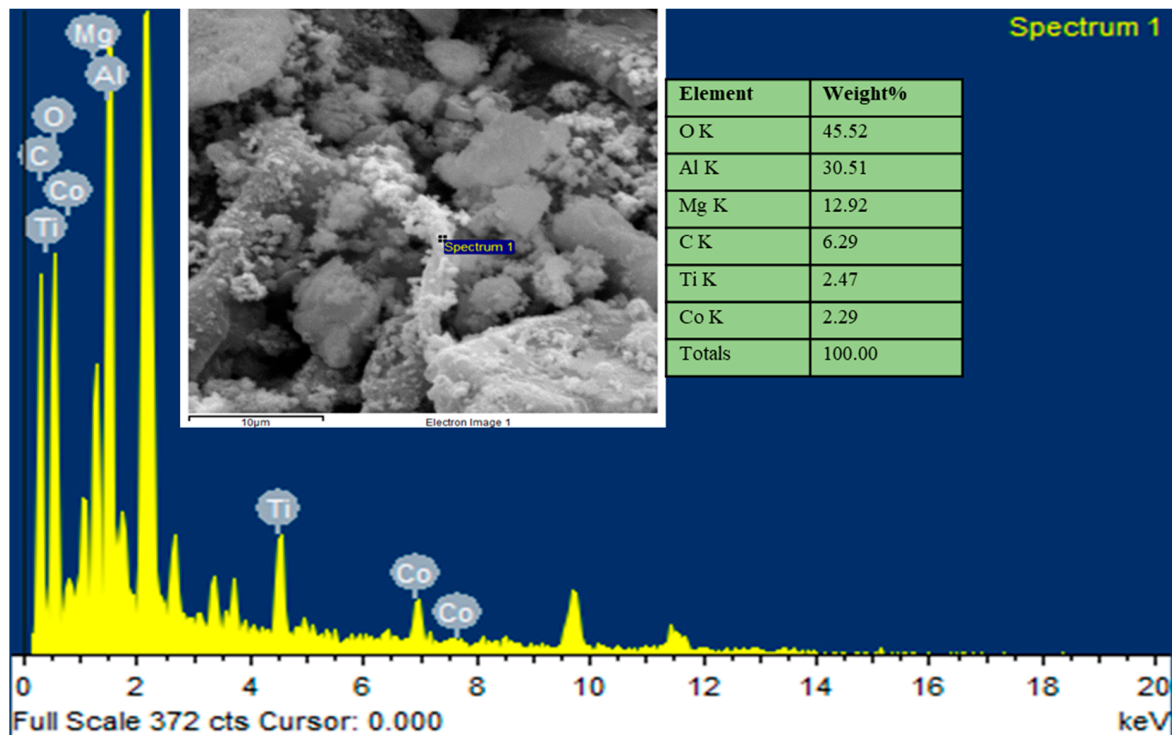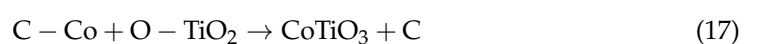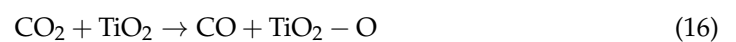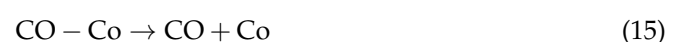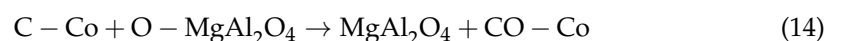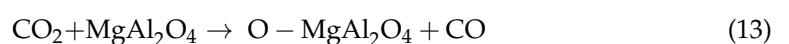
Figure 15. Elemental analysis of spent 5% Co/TiO_2–$MgAl_2O_4$.

The SEM micrograph of the spent catalyst presented in Figure 14c,d shows the support surface that was modified after being exposed to the DRM for 75 h. The carbon presence was confirmed by the elemental analysis, as shown in Figure 15 that indicates the presence of almost 4.5% carbon in the spent catalyst. Though different carbonaceous species were formed due to the reactive phase during the reaction, a carbon gasification at high temperature was expected and produced CO that had a higher syngas ratio.

3.4. Reaction Mechanism

The overall possible reaction mechanism based on the product and spent catalyst analysis is presented in Figure 16. CH_4 activation starts with the adsorption on the active Co surface to produce surface carbon and hydrogen species that then combine to produce hydrogen molecules in the gaseous phase, as represented by reactions (11) and (12) [74,75]. Furthermore, the adsorption of CO_2 onto the supports of TiO_2 and $MgAl_2O_4$ leads to the formation of $CoTiO_3$ species, along with the dissociation of CO_2 to CO, as represented by reactions ((13)–(17)). However, the reaction of surface carbon with the $CoTiO_3$ species may result in the formation of CO, as represented by reaction (18).

$$CH_4 + 2Co \ \rightarrow \ C - Co + H - Co \tag{11}$$

$$2H - Co \ \rightarrow \ H_2 + 2Co \tag{12}$$

$$CO_2 + MgAl_2O_4 \ \rightarrow \ O - MgAl_2O_4 + CO \tag{13}$$

$$C - Co + O - MgAl_2O_4 \rightarrow MgAl_2O_4 + CO - Co \tag{14}$$

$$CO - Co \rightarrow CO + Co \tag{15}$$

$$CO_2 + TiO_2 \rightarrow CO + TiO_2 - O \tag{16}$$

$$C - Co + O - TiO_2 \rightarrow CoTiO_3 + C \tag{17}$$

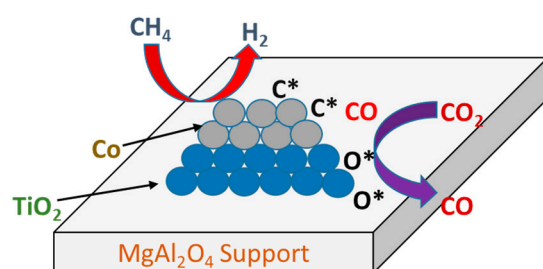$$CoTiO_3 + C \rightarrow Co + TiO_2 + CO \tag{18}$$

Figure 16. Proposed reaction mechanism of the DRM over $Co/TiO_2–MgAl_2O_4$.

4. Conclusions

This study investigated the synthesis of various Co-loaded, $TiO_2–MgAl_2O_4$-supported catalysts for the DRM process in a thermally fixed bed reactor. The $5\%Co/TiO_2–MgAl_2O_4$ showed the best catalytic performance due to its higher CH_4 and CO_2 conversions, improved selectivity, yield of H_2 and CO, and higher stability for more than 75 h TOS. The basic nature of $MgAl_2O_4$ helped the activation and dissociation of CO_2, and the strong metal–support interaction while adding TiO_2 as a co-support. This was evidenced by the formation of $CoTiO_3$ and $CoAl_2O_4$ on the catalyst, which improved the conversion of CH_4 and, consequently, the catalytic performance. Regardless of the highest CH_4 and CO_2 conversions of the $5\%Co/TiO_2–MgAl_2O_4$ among the prepared composites, the H_2/CO ratio was below the theoretical ratio. The reaction of $CoTiO_3$ with the reactive carbon to form TiO_2 and larger amounts of CO brought the H_2/CO ratio to less than unity and improved stability for 75 h TOS. The enhanced stability suggested that this catalyst has prospects for the up-gradation of industrial-scale syngas production when using the DRM process.

Author Contributions: Conceptualization, A.M. and A.H.K.; methodology, A.H.K.; software, S.R.N. and R.L.; validation, S.S., M.H., and M.A.; formal analysis, F.M.; investigation, A.H.K. and M.A.; resources, A.H.K.; data curation, A.K.A.; writing—original draft preparation, A.M. and A.H.K.; writing—review and editing, A.K.A. and S.R.N.; visualization, A.M., R.L.; supervision, A.H.K. and S.R.N. All authors have read and agreed to the published version of the manuscript.

Institutional Review Board Statement: Not applicable.

Informed Consent Statement: Not applicable.

Data Availability Statement: Not applicable.

Conflicts of Interest: The authors declare no conflict of interest.

References

1. Li, X.; Anderson, P.; Jhong, H.-R.M.; Paster, M.; Stubbins, J.F.; Kenis, P.J. Greenhouse gas emissions, energy efficiency, and cost of synthetic fuel production using electrochemical CO_2 conversion and the Fischer–Tropsch process. *Energy Fuels* **2016**, *30*, 5980–5989. [CrossRef]
2. Nawar, A.; Ali, M.; Khoja, A.H.; Waqas, A.; Anwar, M.; Mahmood, M. Enhanced CO_2 capture using organic acid structure modified waste eggshell derived CaO sorbent. *J. Environ. Chem. Eng.* **2021**, *9*, 104871. [CrossRef]
3. Khoja, A.H.; Anwar, M.; Shakir, S.; Mehran, M.T.; Mazhar, A.; Javed, A.; Amin, N.A.S. Thermal dry reforming of methane over La_2O_3 co-supported $Ni/MgAl_2O_4$ catalyst for hydrogen-rich syngas production. *Res. Chem. Intermed.* **2020**, *46*, 3817–3833. [CrossRef]
4. Khoja, A.H.; Tahir, M.; Amin, N.A.S. Recent developments in non-thermal catalytic DBD plasma reactor for dry reforming of methane. *Energy Convers. Manag.* **2019**, *183*, 529–560. [CrossRef]
5. Zaffar, A.; Khan, B.A.; Khoja, A.H.; Khan, U.M.; Sarmad, Q.; Mehran, M.T.; Naqvi, S.R.; Ali, M. Synthesis of Ash Derived Co/Zeolite Catalyst for Hydrogen Rich Syngas Production via Partial Oxidation of Methane. *Bull. Chem. React. Eng. Catal.* **2021**. [CrossRef]

6.   Dan, M.; Mihet, M.; Lazar, M.D. Hydrogen and/or syngas production by combined steam and dry reforming of methane on nickel catalysts. *Int. J. Hydrogen Energy* **2020**, *45*, 26254–26264. [CrossRef]

7.   Khoja, A.H.; Tahir, M.; Amin, N.A.S. Dry reforming of methane using different dielectric materials and DBD plasma reactor configurations. *Energy Convers. Manag.* **2017**, *144*, 262–274. [CrossRef]

8.   Khoja, A.H.; Azad, A.K.; Saleem, F.; Khan, B.A.; Naqvi, S.R.; Mehran, M.T.; Amin, N.A. Hydrogen Production from Methane Cracking in Dielectric Barrier Discharge Catalytic Plasma Reactor Using a Nanocatalyst. *Energies* **2020**, *13*, 5921. [CrossRef]

9.   Abdulrasheed, A.; Jalil, A.A.; Gambo, Y.; Ibrahim, M.; Hambali, H.U.; Hamid, M.Y.S. A review on catalyst development for dry reforming of methane to syngas: Recent advances. *Renew. Sustain. Energy Rev.* **2019**, *108*, 175–193. [CrossRef]

10.   Aziz, M.; Setiabudi, H.; Teh, L.; Annuar, N.; Jalil, A. A review of heterogeneous catalysts for syngas production via dry reforming. *J. Taiwan Inst. Chem. Eng.* **2019**, *101*, 139–158. [CrossRef]

11.   Selvarajah, K.; Phuc, N.H.H.; Abdullah, B.; Alenazey, F.; Vo, D.-V.N. Syngas production from methane dry reforming over Ni/Al$_2$O$_3$ catalyst. *Res. Chem. Intermed.* **2016**, *42*, 269–288. [CrossRef]

12.   Khoja, A.H.; Tahir, M.; Amin, N.A.S. orming of methane over Ni/ɤ-Al$_2$O$_3$ -MgO nanocomposite. *Fuel Process. Technol.* **2018**, *178*, 166–179. [CrossRef]

13.   Abdullah, B.; Ghani, N.A.A.; Vo, D.-V.N. Recent advances in dry reforming of methane over Ni-based catalysts. *J. Clean. Prod.* **2017**, *162*, 170–185. [CrossRef]

14.   Khoja, A.H.; Tahir, M.; Saidina Amin, N.A. Evaluating the Performance of a Ni Catalyst Supported on La$_2$O$_3$-MgAl$_2$O$_4$ for Dry Reforming of Methane in a Packed Bed Dielectric Barrier Discharge Plasma Reactor. *Energy Fuels* **2019**, *33*, 11630–11647. [CrossRef]

15.   Usman, M.; Daud, W.M.A.W. Microemulsion based synthesis of Ni/MgO catalyst for dry reforming of methane. *RSC Adv.* **2016**, *6*, 38277–38289. [CrossRef]

16.   Wu, J.J.; Zhou, X.D. Catalytic conversion of CO$_2$ to value added fuels: Current status, challenges, and future directions. *Chin. J. Catal.* **2016**, *37*, 999–1015. [CrossRef]

17.   Löfberg, A.; Guerrero-Caballero, J.; Kane, T.; Rubbens, A.; Jalowiecki-Duhamel, L. Ni/CeO$_2$ based catalysts as oxygen vectors for the chemical looping dry reforming of methane for syngas production. *Appl. Catal. B Environ.* **2017**, *212*, 159–174. [CrossRef]

18.   Aramouni, N.A.K.; Touma, J.G.; Tarboush, B.A.; Zeaiter, J.; Ahmad, M.N. Catalyst design for dry reforming of methane: Analysis review. *Renew. Sustain. Energy Rev.* **2018**, *82*, 2570–2585. [CrossRef]

19.   Yentekakis, I.V.; Goula, G.; Hatzisymeon, M.; Betsi-Argyropoulou, I.; Botzolaki, G.; Kousi, K.; Kondarides, D.I.; Taylor, M.J.; Parlett, C.M.; Osatiashtiani, A. Effect of support oxygen storage capacity on the catalytic performance of Rh nanoparticles for CO$_2$ reforming of methane. *Appl. Catal. B Environ.* **2019**, *243*, 490–501. [CrossRef]

20.   Wittich, K.; Krämer, M.; Bottke, N.; Schunk, S.A. Catalytic Dry Reforming of Methane: Insights from Model Systems. *ChemCatChem* **2020**. [CrossRef]

21.   García-Diéguez, M.; Pieta, I.; Herrera, M.; Larrubia, M.; Alemany, L. Nanostructured Pt-and Ni-based catalysts for CO$_2$-reforming of methane. *J. Catal.* **2010**, *270*, 136–145. [CrossRef]

22.   Izquierdo, U.; Barrio, V.; Bizkarra, K.; Gutierrez, A.; Arraibi, J.; Gartzia, L.; Bañuelos, J.; Lopez-Arbeloa, I.; Cambra, J. Ni and RhNi catalysts supported on Zeolites L for hydrogen and syngas production by biogas reforming processes. *Chem. Eng. J.* **2014**, *238*, 178–188. [CrossRef]

23.   Tahir, M.; Tahir, B.; Amin, N.A.S.; Muhammad, A. Photocatalytic CO$_2$ methanation over NiO/In$_2$O$_3$ promoted TiO$_2$ nanocatalysts using H$_2$O and/or H$_2$ reductants. *Energy Convers. Manag.* **2016**, *119*, 368–378. [CrossRef]

24.   Zhou, L.; Li, L.; Wei, N.; Li, J.; Basset, J.M. Effect of NiAl2O4 formation on Ni/Al$_2$O$_3$ stability during dry reforming of methane. *ChemCatChem* **2015**, *7*, 2508–2516. [CrossRef]

25.   Das, S.; Thakur, S.; Bag, A.; Gupta, M.S.; Mondal, P.; Bordoloi, A. Support interaction of Ni nanocluster based catalysts applied in CO$_2$ reforming. *J. Catal.* **2015**, *330*, 46–60. [CrossRef]

26.   Christensen, K.O.; Chen, D.; Lødeng, R.; Holmen, A. Effect of supports and Ni crystal size on carbon formation and sintering during steam methane reforming. *Appl. Catal. A Gen.* **2006**, *314*, 9–22. [CrossRef]

27.   Budiman, A.W.; Song, S.-H.; Chang, T.-S.; Shin, C.-H.; Choi, M.-J. Dry reforming of methane over cobalt catalysts: A literature review of catalyst development. *Catal. Surv. Asia* **2012**, *16*, 183–197. [CrossRef]

28.   Ewbank, J.L.; Kovarik, L.; Kenvin, C.C.; Sievers, C. Effect of preparation methods on the performance of Co/Al$_2$O$_3$ catalysts for dry reforming of methane. *Green Chem.* **2014**, *16*, 885–896. [CrossRef]

29.   Abasaeed, A.E.; Al-Fatesh, A.S.; Naeem, M.A.; Ibrahim, A.A.; Fakeeha, A.H. Catalytic performance of CeO$_2$ and ZrO$_2$ supported Co catalysts for hydrogen production via dry reforming of methane. *Int. J. Hydrogen Energy* **2015**, *40*, 6818–6826. [CrossRef]

30.   Ferencz, Z.; Baán, K.; Oszkó, A.; Kónya, Z.; Kecskés, T.; Erdőhelyi, A. Dry reforming of CH$_4$ on Rh doped Co/Al$_2$O$_3$ catalysts. *Catal. Today* **2014**, *228*, 123–130. [CrossRef]

31.   el Hassan, N.; Kaydouh, M.; Geagea, H.; el Zein, H.; Jabbour, K.; Casale, S.; el Zakhem, H.; Massiani, P. Low temperature dry reforming of methane on rhodium and cobalt based catalysts: Active phase stabilization by confinement in mesoporous SBA-15. *Appl. Catal. A Gen.* **2016**, *520*, 114–121. [CrossRef]

32.   Usman, M.; Daud, W.M.A.W.; Abbas, H.F. Dry reforming of methane: Influence of process parameters-A review. *Renew. Sustain. Energy Rev.* **2015**, *45*, 710–744. [CrossRef]

33. Khoja, A.H.; Tahir, M.; Amin, N.A.S. Process optimization of DBD plasma dry reforming of methane over Ni/La2O3MgAl2O4 using multiple response surface methodology. *Int. J. Hydrogen Energy* **2019**, *44*, 11774–11787. [CrossRef]

34. di Michele, A.; Dell'Angelo, A.; Tripodi, A.; Bahadori, E.; Sanchez, F.; Motta, D.; Dimitratos, N.; Rossetti, I.; Ramis, G. Steam reforming of ethanol over Ni/MgAl$_2$O$_4$ catalysts. *Int. J. Hydrogen Energy* **2019**, *44*, 952–964. [CrossRef]

35. Medeiros, R.L.; Macedo, H.P.; Melo, V.R.; Oliveira, Â.A.; Barros, J.M.; Melo, M.A.; Melo, D.M. Ni supported on Fe-doped MgAl$_2$O$_4$ for dry reforming of methane: Use of factorial design to optimize H$_2$ yield. *Int. J. Hydrogen Energy* **2016**, *41*, 14047–14057. [CrossRef]

36. Safari, J.; Akbari, Z.; Naseh, S. Nanocrystalline MgAl$_2$O$_4$ as an efficient catalyst for one-pot synthesis of multisubstituted imidazoles under solvent-free conditions. *J. Saudi Chem. Soc.* **2016**, *20*, S250–S255. [CrossRef]

37. Hadian, N.; Rezaei, M.; Mosayebi, Z.; Meshkani, F. CO$_2$ reforming of methane over nickel catalysts supported on nanocrystalline MgAl2O4 with high surface area. *J. Nat. Gas Chem.* **2012**, *21*, 200–206. [CrossRef]

38. Seo, H.O.; Sim, J.K.; Kim, K.-D.; Kim, Y.D.; Lim, D.C.; Kim, S.H. Carbon dioxide reforming of methane to synthesis gas over a TiO$_2$–Ni inverse catalyst. *Appl. Catal. A Gen.* **2013**, *451*, 43–49. [CrossRef]

39. Abbas, T.; Tahir, M.; Saidina Amin, N.A. Enhanced metal–support interaction in Ni/Co$_3$O$_4$/TiO$_2$ nanorods toward stable and dynamic hydrogen production from phenol steam reforming. *Ind. Eng. Chem. Res.* **2018**, *58*, 517–530. [CrossRef]

40. Kho, E.T.; Scott, J.; Amal, R. Ni/TiO$_2$ for low temperature steam reforming of methane. *Chem. Eng. Sci.* **2016**, *140*, 161–170. [CrossRef]

41. Shehzad, N.; Tahir, M.; Johari, K.; Murugesan, T.; Hussain, M. A critical review on TiO$_2$ based photocatalytic CO$_2$ reduction system: Strategies to improve efficiency. *J. CO$_2$ Util.* **2018**, *26*, 98–122. [CrossRef]

42. Mosayebi, Z.; Rezaei, M.; Hadian, N.; Kordshuli, F.Z.; Meshkani, F. Low temperature synthesis of nanocrystalline magnesium aluminate with high surface area by surfactant assisted precipitation method: Effect of preparation conditions. *Mater. Res. Bull.* **2012**, *47*, 2154–2160. [CrossRef]

43. Nor, A.M.; Achoi, M.F.; Mamat, M.H.; Zabidi, M.M.; Abdullah, S.; Mahmood, M.R. Synthesis of TiO$_2$ nanowires via hydrothermal method. *Jpn. J. Appl. Phys.* **2012**, *51*, 06FG08. [CrossRef]

44. Charisiou, N.; Siakavelas, G.; Papageridis, K.; Baklavaridis, A.; Tzounis, L.; Avraam, D.; Goula, M. Syngas production via the biogas dry reforming reaction over nickel supported on modified with CeO$_2$ and/or La$_2$O$_3$ alumina catalysts. *J. Nat. Gas Sci. Eng.* **2016**, *31*, 164–183. [CrossRef]

45. Munawar, M.A.; Khoja, A.H.; Hassan, M.; Liaquat, R.; Naqvi, S.R.; Mehran, M.T.; Abdullah, A.; Saleem, F. Biomass ash characterization, fusion analysis and its application in catalytic decomposition of methane. *Fuel* **2021**, *285*, 119107. [CrossRef]

46. Saberi, A.; Golestani-Fard, F.; Sarpoolaky, H.; Willert-Porada, M.; Gerdes, T.; Simon, R.; Liebscher, C. Development of MgAl2O4 spinel coating on graphite surface to improve its water-wettability and oxidation resistance. *Ceram. Int.* **2009**, *35*, 457–461. [CrossRef]

47. Jiao, Y.; Chen, T.; Wang, L.; Yao, P.; Zhang, J.; Chen, Y.; Chen, Y.; Wang, J. Synthesis of a High-Stability Nanosized Pt-Loaded MgAl$_2$O$_4$ Catalyst for n-Decane Cracking with Enhanced Activity and Durability. *Ind. Eng. Chem. Res.* **2020**, *59*, 4338–4347. [CrossRef]

48. Maruthapandi, M.; Eswaran, L.; Luong, J.H.; Gedanken, A. Sonochemical preparation of polyaniline@ TiO2 and polyaniline@ SiO2 for the removal of anionic and cationic dyes. *Ultrason. Sonochem.* **2020**, *62*, 104864. [CrossRef] [PubMed]

49. Wang, Y.; Wang, S.; Yu, X.; Tang, S.; Han, S.; Yang, L. Irradiation synthesis and characterization of CoAl$_2$O$_4$: Ce and Mn-codoped CoAl$_2$O$_4$: Ce phosphors. *Optik* **2020**, *210*, 164508. [CrossRef]

50. Zhou, Y.; Wang, Y.; Wang, J.; Lin, L.; Wu, X.; He, D. Controlled synthesis and characterization of hybrid Sn-doped Co$_3$O$_4$ nanowires for supercapacitors. *Mater. Lett.* **2018**, *216*, 248–251. [CrossRef]

51. Wang, Q.; Guo, Q.; Wang, L.; Li, B. The flux growth of single-crystalline CoTiO$_3$ polyhedral particles and improved visible-light photocatalytic activity of heterostructured CoTiO$_3$/gC$_3$N$_4$ composites. *Dalton Trans.* **2016**, *45*, 17748–17758. [CrossRef] [PubMed]

52. Tahir, M.N.; Andre, R.; Sahoo, J.K.; Jochum, F.D.; Theato, P.; Natalio, F.; Berger, R.; Branscheid, R.; Kolb, U.; Tremel, W. Hydrogen peroxide sensors for cellular imaging based on horse radish peroxidase reconstituted on polymer-functionalized TiO$_2$ nanorods. *Nanoscale* **2011**, *3*, 3907–3914. [CrossRef] [PubMed]

53. Thanabodeekij, N.; Sathupunya, M.; Jamieson, A.M.; Wongkasemjit, S. Correlation of sol–gel processing parameters with microstructure and properties of a ceramic product. *Mater. Charact.* **2003**, *50*, 325–337. [CrossRef]

54. Adak, A.; Saha, S.; Pramanik, P. Synthesis and characterization of MgAl 2 O 4 spinel by PVA evaporation technique. *J. Mater. Sci. Lett.* **1997**, *16*, 234–235. [CrossRef]

55. Sanjabi, S.; Obeydavi, A. Synthesis and characterization of nanocrystalline MgAl$_2$O$_4$ spinel via modified sol–gel method. *J. Alloys Compd.* **2015**, *645*, 535–540. [CrossRef]

56. Tai, J.Y.; Leong, K.H.; Saravanan, P.; Aziz, A.A.; Sim, L.C. Dopant-free oxygen-rich titanium dioxide: LED light-induced photocatalysis and mechanism insight. *J. Mater. Sci.* **2017**, *52*, 11630–11642. [CrossRef]

57. Etacheri, V.; Seery, M.K.; Hinder, S.J.; Pillai, S.C. Oxygen rich titania: A dopant free, high temperature stable, and visible-light active anatase photocatalyst. *Adv. Funct. Mater.* **2011**, *21*, 3744–3752. [CrossRef]

58. Sim, L.C.; Tan, W.H.; Leong, K.H.; Bashir, M.J.; Saravanan, P.; Surib, N.A. Mechanistic characteristics of surface modified organic semiconductor g-C$_3$N$_4$ nanotubes alloyed with titania. *Materials* **2017**, *10*, 28. [CrossRef] [PubMed]

59. Prabaharan, D.D.M.; Sadaiyandi, K.; Mahendran, M.; Sagadevan, S. Precipitation method and characterization of cobalt oxide nanoparticles. *Appl. Phys. A* **2017**, *123*, 264. [CrossRef]

60. Domínguez, A.; Fernández, Y.; Fidalgo, B.; Pis, J.; Menéndez, J. Biogas to syngas by microwave-assisted dry reforming in the presence of char. *Energy Fuels* **2007**, *21*, 2066–2071. [CrossRef]

61. Tavasoli, A.; Sadaghiani, K.; Nakhaeipour, A.; Ahangari, M. Cobalt loading effects on the structure and activity for Fischer-Tropsch and water-gas shift reactions of Co/Al2O3 catalysts. *Iran. J. Chem. Chem. Eng.* **2007**, *26*, 9–16.

62. Wang, W.-J.; Chen, Y.-W. Influence of metal loading on the reducibility and hydrogenation activity of cobalt/alumina catalysts. *Appl. Catal.* **1991**, *77*, 223–233. [CrossRef]

63. Zhang, G.; Su, A.; Du, Y.; Qu, J.; Xu, Y. Catalytic performance of activated carbon supported cobalt catalyst for CO_2 reforming of CH_4. *J. Colloid Interface Sci.* **2014**, *433*, 149–155. [CrossRef] [PubMed]

64. Baamran, K.S.; Tahir, M. Ni-embedded TiO_2-$ZnTiO_3$ reducible perovskite composite with synergistic effect of metal/support towards enhanced H2 production via phenol steam reforming. *Energy Convers. Manag.* **2019**, *200*, 112064. [CrossRef]

65. Zhang, J.; Wang, H.; Dalai, A.K. Effects of metal content on activity and stability of Ni-Co bimetallic catalysts for CO_2 reforming of CH4. *Appl. Catal. A Gen.* **2008**, *339*, 121–129. [CrossRef]

66. Seo, H.O. Recent scientific progress on developing supported Ni catalysts for dry (CO_2) reforming of methane. *Catalysts* **2018**, *8*, 110. [CrossRef]

67. Takanabe, K.; Nagaoka, K.; Nariai, K.; Aika, K. Influence of reduction temperature on the catalytic behavior of Co/TiO_2 catalysts for CH4/CO2 reforming and its relation with titania bulk crystal structure. *J. Catal.* **2005**, *230*, 75–85. [CrossRef]

68. Nagaoka, K.; Takanabe, K.; Aika, K. Modification of Co/TiO_2 for dry reforming of methane at 2 MPa by Pt, Ru or Ni. *Appl. Catal. A Gen.* **2004**, *268*, 151–158. [CrossRef]

69. Xu, L.; Zhang, J.; Wang, F.; Yuan, K.; Wang, L.; Wu, K.; Xu, G.; Chen, W. One-step synthesis of ordered mesoporous $CoAl_2O_4$ spinel-based metal oxides for CO_2 reforming of CH_4. *RSC Adv.* **2015**, *5*, 48256–48268. [CrossRef]

70. Salvador, F.; Sánchez-Montero, M.J.; Izquierdo, C. C/H_2O reaction under supercritical conditions and their repercussions in the preparation of activated carbon. *J. Phys. Chem. C* **2007**, *111*, 14011–14020. [CrossRef]

71. Guler, M.; Dogu, T.; Varisli, D. Hydrogen production over molybdenum loaded mesoporous carbon catalysts in microwave heated reactor system. *Appl. Catal. B Environ.* **2017**, *219*, 173–182. [CrossRef]

72. Chong, C.C.; Setiabudi, H.D.; Jalil, A.A. Dendritic fibrous SBA-15 supported nickel (Ni/DFSBA-15): A sustainable catalyst for hydrogen production. *Int. J. Hydrogen Energy* **2020**, *45*, 18533–18548. [CrossRef]

73. Al-Fatesh, A.S.; Naeem, M.A.; Fakeeha, A.H.; Abasaeed, A.E. Role of La_2O_3 as promoter and support in Ni/γ-Al_2O_3 catalysts for dry reforming of methane. *Chin. J. Chem. Eng.* **2014**, *22*, 28–37. [CrossRef]

74. Fan, M.S.; Abdullah, A.Z.; Bhatia, S. Catalytic technology for carbon dioxide reforming of methane to synthesis gas. *ChemCatChem* **2009**, *1*, 192–208. [CrossRef]

75. Topalidis, A.; Petrakis, D.; Ladavos, A.; Loukatzikou, L.; Pomonis, P. A kinetic study of methane and carbon dioxide interconversion over 0.5% Pt/$SrTiO_3$ catalysts. *Catal. Today* **2007**, *127*, 238–245. [CrossRef]